1-1-2012

Multicomponent cubic oxide exsolution in synthetic basalts: Temperature dependence and implications for magnetic properties

Julie A. Bowles
University of Wisconsin-Milwaukee, bowlesj@uwm.edu

Lisa Tatsumi-Petrochilos
University of Hawaii, Manoa

Julie E. Hammer
University of Hawaii, Manoa

Stefanie A. Brachfeld
Montclair State University, brachfelds@mail.montclair.edu

Multicomponent cubic oxide exsolution in synthetic basalts: Temperature dependence and implications for magnetic properties

Julie A. Bowles,[1] Lisa Tatsumi-Petrochilos,[2] Julia E. Hammer,[2] and Stefanie A. Brachfeld[3]

Received 14 September 2011; revised 27 December 2011; accepted 3 January 2012; published 8 March 2012.

[1] Although the compositional unmixing of cubic-structured iron oxides has profound effects on the magnetic properties of rocks that contain them, a basic understanding of the kinetics and thermodynamics of this process has not been achieved in experimental studies due to sluggish reaction rates in binary oxide phases. Exploiting the fact that many natural Fe-oxides contain multiple additional cations, including Ti, Mg and Al, we perform novel "forward" laboratory experiments in which cubic-cubic phase exsolution proceeds from initially homogeneous multicomponent oxides. A variety of Fe-Ti-Mg-Al cubic iron oxides were nucleated and grown in synthetic, multicomponent basalt under different fO_2 environments, and annealed at temperatures ranging from 590–790°C for up to 88 days. Fine-scale lamellar intergrowths of Fe-Ti-Al-Mg oxides, interpreted to represent cubic phase exsolution, were observed in seven samples, one that was synthesized and annealed at approximately constant fO_2 (the quartz-fayalite-magnetite, or QFM, buffer) and six that were synthesized at very oxidizing conditions (∼QFM + 6 log units) and then annealed at moderately oxidizing (∼QFM) conditions. Results demonstrate that the consolute temperature of the multicomponent system is significantly higher than anneal temperatures and Curie temperatures, suggesting that samples that undergo this type of exsolution can carry a total thermal remanent magnetization. Exsolved samples are characterized by a dramatic increase in magnetization and coercivity, and a shift in Curie temperature(s), confirming predictions that this type of exsolution exerts strong control on the strength and stability of magnetization.

Citation: Bowles, J. A., L. Tatsumi-Petrochilos, J. E. Hammer, and S. A. Brachfeld (2012), Multicomponent cubic oxide exsolution in synthetic basalts: Temperature dependence and implications for magnetic properties, *J. Geophys. Res.*, *117*, B03202, doi:10.1029/2011JB008867.

1. Introduction

[2] So long as cooling occurs slowly and the environment is not overly oxidizing, oxide minerals undergo exsolution to produce finely intergrown phases that are closer in composition to end-member components than the original crystal. Titanomagnetite ($Fe_{3-x}Ti_xO_4$, $0 \leq x \leq 1$) exsolution is the most commonly cited example and is observed in massive ore deposits and mafic plutons [*Price*, 1980]. However, it is comparatively rare because oxidizing conditions in the Earth's crust favor the so-called oxy-exsolution of titanomagnetite (TM) to produce ilmenite lamellae in magnetite [*Haggerty*, 1991]. One important consequence of exsolution *sensu stricto* is a change in magnetic properties. Upon unmixing of TM, small particles of near-pure magnetite become separated by non-magnetic ulvöspinel matrix [*Hargraves et al.*, 2001], leading to a smaller magnetic domain size and an increase in Curie temperature. Combined, these properties are predicted to result in a stronger, more stable magnetization [*Hargraves et al.*, 2001].

[3] Because Fe-Ti cubic oxides in most natural rocks also contain some Mg and Al [*Deer et al.*, 1962; *Frost and Lindsley*, 1991], a key to understanding the consequences for magnetic properties of oxide exsolution is determining the temperature-composition surface of the Fe-Mg-Al-Ti cubic oxide solvus. The low temperature of cubic oxide exsolution presents a challenge to laboratory study [*Harrison and Putnis*, 1998]. One approach is to anneal naturally exsolved titanomagnetite or synthetic mixtures of magnetite and ulvöspinel at various temperatures and durations to drive homogenization of the two phases [*Evans et al.*, 2006; *Kawai*, 1956; *Price*, 1981; *Vincent et al.*, 1957]. These "reverse" experiments provide constraints on the shape and temperature of the binary solvus. However, "forward"

[1]Institute for Rock Magnetism, Department of Earth Sciences, University of Minnesota, Twin Cities, Minneapolis, Minnesota, USA.
[2]Department of Geology and Geophysics, University of Hawai'i at Mānoa, Honolulu, Hawaii, USA.
[3]Department of Earth and Environmental Studies, Montclair State University, Upper Montclair, New Jersey, USA.

0148-0227/12/2011JB008867

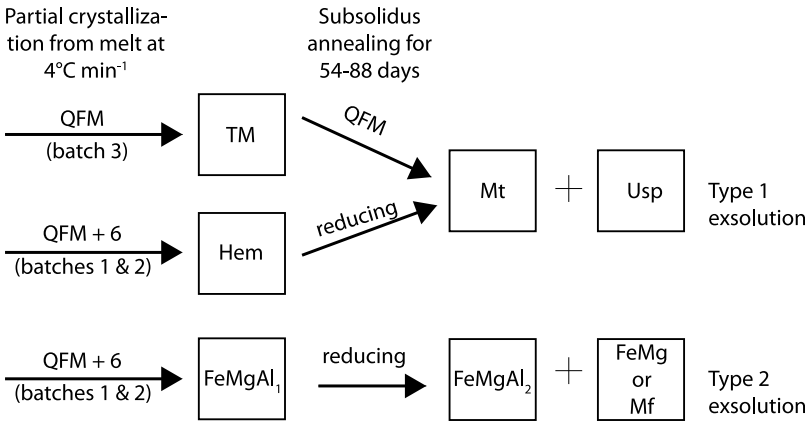

Figure 1. Schematic representation of experimental workflow and resulting exsolution products. Usp, ülvospinel. Hem, hematite. Mt, magnetite. $FeMgAl_1$ and $FeMgAl_2$, Fe-Mg-Al cubic oxides. FeMg, Fe-Mg cubic oxide. Mf, magnesioferrite. See text or Table 3 for exact compositions.

experiments, in which an initially homogeneous grain is held at subsolvus temperature and undergoes exsolution, are needed to address the chemical reaction pathway and rate at which exsolution occurs in nature. The only prior experiments of this type involve the magnetite (Fe_3O_4)-spinel ($MgAl_2O_4$) solid solution [*Harrison and Putnis*, 1997] and the magnetite-hercynite ($FeAl_2O_4$) solid solution [*Golla-Schindler et al.*, 2005].

[4] A related issue is whether exsolution occurs above the Curie temperature (T_c) of the exsolved magnetic grains, which then can acquire a total thermal remanent magnetization (TRM). Existing constraints on the Fe_3O_4- Fe_2TiO_4 binary solvus [*Kawai*, 1956; *Lindsley*, 1981; *Price*, 1981; *Vincent et al.*, 1957] suggest that the solvus crest (consolute) temperature is low (<600°C) with respect to the Curie temperatures in this system. Thus, only TM compositions that exsolve promptly upon cooling through the solvus (in the temperature range of ~450–600°C) can produce a magnetite-rich phase with a total TRM. In contrast, the consolute temperature in the Fe_3O_4-$FeAl_2O_4$ (hercynite) solid solution is considerably higher, ~850°C [*Turnock and Eugster*, 1962], and that of Fe_3O_4-$MgAl_2O_4$ (spinel) is 900–1000°C [*Mattioli and Wood*, 1988], suggesting a greater likelihood that multicomponent cubic oxides acquire a TRM during cooling.

[5] Hoping to exploit a tendency for multicomponent oxides to unmix at higher temperatures than binary oxides, we synthesized basalts, saturated them with Fe-Mg-Al-Ti oxides and subjected them to protracted subsolidus conditions (590°C–790°C) in order to (a) determine whether exsolution occurs on a laboratory time scale (54–88 days), and (b) characterize the microtextural, compositional, and magnetic properties of the "annealed" materials. The bulk compositions, desired oxygen environment, and thermal histories applied in the synthesis of starting materials were selected for their relevance to prior studies of igneous materials capable of acquiring and sustaining intense thermoremanent magnetization in the crust of Mars [*Bowles et al.*, 2009; *Brachfeld and Hammer*, 2006; *Hammer et al.*, 2006]. First, basalts were synthesized and partially crystallized in dynamic cooling experiments (Figure 1) using two starting compositions, one with high Fe/Al (designated M-type), and the other with lower Fe/Al (T-type). All syntheses were intended to take place at the QFM buffer, but several lines of evidence (described below) indicate that fO_2 conditions during four out of six synthesis runs exceeded the QFM buffer by 6–7 log units. Second, the partly crystalline basalts were annealed at subsolidus temperatures (Figure 1) near QFM buffering conditions for up to 88 days. Thus, some of the materials were synthesized at extremely oxidizing conditions and then subjected to a significant reduction in fO_2 during the long-duration anneal runs, while others were synthesized and annealed at steady conditions with respect to the QFM buffer.

[6] Most of the phase assemblages produced during synthesis of the partly crystalline pre-anneal material, notably including magnesioferrite-rich cubic oxide and titanohematite rhombohedral oxide, have no plausible connection to the Martian crust. However, because both phases are present in terrestrial rocks, our results may be applicable to geological environments on Earth. Nearly identical natural magnesioferrite-rich oxides form in the Earth's mantle [*Wood and Virgo*, 1989; *Tamura and Arai*, 2005], in meteorite fusion crusts [*Genge and Grady*, 1999] and impact melts [e.g., *Smit*, 1999], and in alkalic ocean island gabbros [*Johnston and Stout*, 1984], and even arc trachyandesite lavas [*Shi et al.*, 2009]. The commonality of these diverse rock types is highly oxidizing crystallization environments (up to QFM + 7), which elevate melt Fe^{3+}/Fe^{2+} and stabilize oxides that are Mg-rich. Likewise, igneous hematite is associated with highly oxidizing conditions in the Earth's crust.

[7] We present the results of a combined petrologic and magnetic characterization of the run products in order to document texturally, magnetically, and as a function of anneal temperature, that exsolution occurred in both oxide phases present in the starting material – something that has rarely been done in a laboratory "forward" experiment. We consider the relative importance of oxidation-reduction in the generation of cubic Fe_3O_4-rich lamellae from a rhombohedral hematite-rich precursor, and then discuss available constraints on the position of the multicomponent solvus, its position relative to the T_c surface, and implications of the

Table 1. Partly Crystalline Pre-anneal Material

Sample ID	Composition[a]	Batch	fO_2 (ΔQFM)
MAm-36	M	1	6
MAm-37	M	2	6
MAm-51	M	3	0
MB2-31	T	1	6
MB2-33	T	2	6
MB2-48	T	3	0

[a]M = M-type (Fe/Al = 1.5); T = T-type (Fe/Al = 0.35). See *Bowles et al.* [2009].

exsolution for bulk magnetic properties including domain state and saturation magnetization.

2. Methods

[8] Reagent oxide powder mixtures were first conditioned at QFM under flowing H_2-CO_2 gas at 925°C. Samples were then melted and partly crystallized during controlled cooling at 4°C/h from the liquidus to 1070°C, at which temperature samples remained for 35–100 h in order to coarsen the oxide grains. This partial crystallization was done in three batches in order to produce enough material for the anneal runs (Table 1). During crystallization, samples were contained either in small, Fe-saturated Pt capsules sealed within evacuated silica glass tubes (Batches 1 and 2) or in a larger, Fe-saturated Pt crucible under flowing H_2-CO_2 gas (Batch 3). We suspect that diffusion of oxygen through the enclosing silica-glass tubes during the coarsening step is responsible for the high degree of oxidation in Batches 1 and 2 (described below). Although the fO_2 value corresponding to the fayalite-quartz-magnetite buffer is relevant to a range of natural crystallization environments, the assemblage has a relatively low buffering capacity because so much of its mass is allocated to SiO_2, the phase with no direct redox potential. Although we verified through visual inspection of crushed grains that some fayalite remained at the end of these runs, we suspect a reaction rind of magnetite + quartz shielded fayalite from participation in the oxidation reaction. The batch conditioned using H_2-CO_2 gas flow evidently suffered no such excursion to high fO_2 values.

[9] Splits from these partly crystalline basalts were sealed in Ag capsules, which in turn were sealed in evacuated quartz tubes along with Fe^0 powder intended to serve as an oxygen getter. Samples were annealed at temperatures between 590°C and 790°C, for 54 to 88 days (Table 2).

[10] Electron backscatter images and nonquantitative EDS constraints on mineral compositions were acquired on all samples with a JEOL J5900 scanning electron microscope (SEM) at University of Hawaii. Electron probe microanalyses (EPMA) (and higher-resolution backscatter images) were obtained using a JEOL JXA-8500F Field Emission Hyperprobe, also at University of Hawaii. EMPA analyses were restricted to a subset of samples annealed at the highest temperatures (and their pre-anneal materials), as these samples represent the closest approximation to exsolution end-member compositions. Cations measured were Fe, Ti, Mg, Al, Mn, and Cr. Probe conditions include accelerating voltage of 15 kV, 8–25 nA beam current, with lower values selected for spatially heterogeneous crystals. A focused beam (≤1 um spot) was utilized on most crystals, owing to the extremely close spacing of lamellae and/or fine grain size. Compositions were obtained from raw x-ray counts using a ZAF-PAP intensity correction [*Joy*, 2001; *Reed*, 1993]. A magnetite standard (NMNH 114887) was used both to calibrate Fe and as a bench standard to verify the calibration. Analyses of this standard yielded totals (uncorrected for Fe speciation) that are consistently 1–2 wt.% low. Close inspection of this standard afforded by the high-resolution BSE imaging capability of the JEOL hyperprobe reveals compositional heterogeneities, which may contribute to the low totals in the analyses of this material as well as the experimental samples. A variety of other factors associated with EPMA analysis of these challenging materials may also contribute to the observed (upward and downward) deviations of oxide totals from 100%. These include vacancies or excess oxygen, secondary fluorescence from neighboring lamellae or phase boundaries [*Llovet and Galan*, 2003], interaction volumes that span across exsolution lamellae or other small scale spatial heterogeneities, charging effects, and beam deflection associated with magnetic materials. Rhombohedral or cubic oxide structure was inferred by selecting the mineral formula (3 or 4 oxygens) that yielded totals closest to 100% using the scheme of *Droop* [1987]. Corrected totals for most analyses were 100% ± 4%. Structure determinations were corroborated by Raman spectroscopy, which displays distinctive features dependent on mineral structure [e.g., *de Faria et al.*, 1997; *Wang et al.*, 2004; *Zinin et al.*, 2011], and were spot checked on a small number of samples with electron backscatter diffraction (EBSD). Atomic force microscopy (AFM) and magnetic force microscopy (MFM) measurements were made on a subset of samples using a Digital Instruments Nanoscope at the Institute for Rock Magnetism (IRM), University of Minnesota.

[11] Splits from all pre- and post-anneal samples were used for magnetic analyses. Hysteresis loops (M-vs-H) were measured on a vibrating sample magnetometer (VSM) in a maximum field of 1 T. First order reversal curves (FORC) [e.g., *Pike et al.*, 1999] were also measured on a VSM using a saturating field of 1.7 T. Ordering temperatures >25°C were determined by measuring induced magnetization (in a 50 mT field) continuously as a function of temperature in flowing He gas. Although the same ordering temperatures appeared in both heating and cooling curves at approximately the same temperatures, some samples had a significant (up to 55%, but most <20%) change in saturation magnetization (M_s) over the course of heating. For this reason, ordering temperatures were calculated using the method of intersecting tangents [*Grommé et al.*, 1969] on heating-only data. Percent change in M_s for all specimens is given in the auxiliary material, Table S1.[1]

3. Results

3.1. Microscopy

3.1.1. Compositions, Textures, and Oxidation State of Pre-anneal Materials

[12] The two dominant oxides that crystallized from the liquid during preparation of both M-type and T-type

[1]Auxiliary material data sets are available at ftp://ftp.agu.org/apend/jb/2011jb008867. Other auxiliary material files are in the HTML.

Table 2. Anneal Conditions

Sample ID	Pre-anneal Material	Batch	Anneal Temperature (°C)	Anneal Time (days)
MAm-E-03	MAm-36	1	710	54
MAm-E-04	MAm-36	1	650	72
MAm-E-05	MAm-37	2	630	84
MAm-E-06	MAm-37	2	590	84
MAm-E-14	MAm-51	3	790	88
MAm-E-15	MAm-51	3	750	88
MB2-E-03	MB2-31	1	710	54
MB2-E-04	MB2-31	1	650	72
MB2-E-05	MB2-33	2	630	72
MB2-E-06	MB2-33	2	590	72
MB2-E-14	MB2-48	3	790	88
MB2-E-15	MB2-48	3	750	88

Batch 1 pre-anneal material are a cubic Fe-Mg-Al oxide ($Fe_{1.9}Mg_{0.7}Al_{0.2}Z_{0.2}O_4$, where Z represents all other cations with <0.2 contribution) and a hematite-rich rhombohedral phase ($Fe_{1.7}Z_{0.3}O_3$) (Table 3). Magnetic properties indicate that Batch 2 pre-anneal materials are very similar to Batch 1 (below). The compositions of the coexisting oxides indicate an oxygen fugacity of QFM + 6 (QUIlF model [*Andersen et al.*, 1993]). M-type hematites are commonly 1–30 μm in diameter, with smaller crystals mostly euhedral and equant, and larger crystals hoppered or anhedral. M-type cubic oxides are commonly equant, euhedral, and 1–30 μm in diameter. T-type oxides are more commonly dendritic and typically smaller (1–5 μm), with a few crystals up to ~70 μm in diameter. The complete phase assemblage in M-type samples (in order of decreasing volumetric abundance) is clinopyroxene, glass, hematite, cubic Fe-Mg-Al oxide, and plagioclase. In T-type samples it is plagioclase, clinopyroxene, glass, cubic Fe-Mg-Al oxide, and hematite.

[13] Batch 3 M-type starting materials crystallized only one cubic oxide phase, a Mg- and Al-bearing titanomagnetite ($Fe_{2.4}Ti_{0.4}Z_{0.2}O_4$, Table 3). Most crystals are 30–80 μm in diameter and are equant and euhedral or skeletal. A subordinate population of smaller (5–15 μm), rounded, equant crystals is also present. Batch 3 T-type starting materials crystallized an ulvöspinel-rich cubic oxide ($Fe_{2.0}Ti_{0.5}Mg_{0.3}Al_{0.2}O_4$) and an ilmenite-rich rhombohedral oxide ($Fe_{0.9}Ti_{0.8}Mg_{0.2}Z_{0.1}O_3$). Titanomagnetite crystals are euhedral, equant, and ~5–10 μm in diameter, while ilmenite crystals are euhedral, elongated and ~5 × 30 μm. Oxide compositions indicate that QFM was maintained during preparation of both starting materials (QUIlF model [*Andersen et al.*, 1993]). The complete phase assemblage (in approximate

Table 3. Oxide Compositions[a]

					Cubic Oxides												
					Composition on a Cation Basis						Percent End-Member Compositions						
Sample ID	P/A	Batch	Exol Type	N	Fe[b]	Ti[b]	Mg[b]	Al[b]	Mn[b]	Cr[b]	Mt	Usp	Mf	Sp	Hc	Jc	Cr
MAm-36	P	1	NA	7	1.93	0.04	0.7	0.23	0.07	0.03	17.7	4.0	58.3	11.6	0.0	7.0	1.4
MAm-51	P	3	NA	20	2.36	0.37	0.11	0.13	0.02	0.00	49.6	37.4	4.4	6.7	0.0	1.8	0.1
MAm-E-03	A	1	1	2	2.55	0.25	0.07	0.11	0.02	0.01	66.2	24.6	1.5	5.4	0.0	2.0	0.3
MAm-E-03	A	1	1	5	2.72	0.12	0.08	0.06	0.02	0.01	78.2	11.8	5.0	2.8	0.0	1.8	0.5
MAm-E-03	A	1	2[c]	8	2.2	0.05	0.38	0.2	0.03	0.13	46.3	5.5	28.6	9.8	0.0	3.2	6.7
MAm-E-03	A	1	NA	7	2.12	0.03	0.44	0.24	0.05	0.13	42.1	2.8	32.2	11.9	0.0	4.7	6.3
MAm-E-14	A	3	1	5	2.65	0.24	0.02	0.09	0.01	0.00	71.2	23.6	0.0	2.1	2.3	0.8	0.0
MAm-E-14	A	3	1	4	2.20	0.53	0.02	0.24	0.01	0.00	34.1	53.2	0.0	2.3	9.5	1.0	0.1
MAm-E-14	A	3	NA	4	2.42	0.38	0.03	0.15	0.02	0.00	52.8	38.0	0.0	2.8	4.9	1.6	0.0
MAm-E-15	A	3	NA	9	2.45	0.34	0.04	0.15	0.01	0.01	56.6	34.2	0.2	3.6	3.8	1.2	0.5
MB2-31	P	1	NA	9	1.99	0.06	0.66	0.18	0.07	0.03	19.0	5.9	57.1	8.9	0.0	7.3	1.7
MB2-48	P	3	NA	17	2.04	0.46	0.26	0.15	0.04	0.04	21.2	46.3	19.1	7.4	0.0	4.1	1.9
MB2-E-03	A	1	2a	2	2.37	0.02	0.47	0.08	0.03	0.03	46.8	1.9	42.7	4.1	0.0	2.9	1.7
MB2-E-03	A	1	2a	2	2.25	0.05	0.33	0.26	0.03	0.08	52.3	4.8	19.7	12.9	0.0	2.7	7.6
MB2-E-03	A	1	2b	2	2.16	0.08	0.46	0.2	0.07	0.03	37.5	7.9	36.3	10.0	0.0	6.9	1.4
MB2-E-03	A	1	2b	2	1.90	0.06	0.81	0.13	0.08	0.03	4.2	5.7	74.9	6.4	0.0	7.5	1.3
MB2-E-03	A	1	NA	2	2.00	0.06	0.66	0.16	0.08	0.04	18.3	6.5	57.7	8.0	0.0	7.5	2.0
MB2-E-14	A	3	NA	4	2.09	0.42	0.18	0.17	0.04	0.10	30.8	42.0	9.8	8.1	0.2	4.1	5.1
MB2-E-15	A	3	NA	10	2.06	0.47	0.14	0.14	0.04	0.15	27.9	46.7	7.0	7.0	0.1	3.8	7.5

					Rhombohedral Oxides										
					Composition on a Cation Basis						Percent End-Member Compositions				
Sample ID	P/A	Batch	Exol Type	N	Fe[b]	Ti[b]	Mg[b]	Al[b]	Mn[b]	Cr[b]	Hm	Ilm	Gk	Py	Es
MAm-36	P	1	NA	9	1.72	0.11	0.09	0.06	0.01	0.01	87.8	1.1	9.1	1.3	0.7
MB2-31	P	1	NA	4	1.65	0.16	0.11	0.05	0.01	0.02	82.7	3.9	10.9	1.3	1.1
MB2-48	P	3	NA	6	0.91	0.84	0.20	0.02	0.02	0.00	15.2	61.5	20.7	2.5	0.2
MB2-E-14	A	3	NA	2	0.94	0.89	0.09	0.04	0.03	0.01	8.7	79.0	8.8	3.1	0.4
MB2-E-15	A	3	NA	1	0.91	0.94	0.08	0.03	0.03	0.01	3.9	84.6	8.1	2.7	0.8

[a]P/A, pre-anneal or annealed material. Exol Type, exsolution type referred to in text; 2a refers to the Fe-Mg/Fe-Mg-Al exsolution, while 2b refers to Mg/Fe-Mg-Al exsolution. N, number of spot analyses averaged. Mt, magnetite (Fe_3O_4). Usp, ulvöspinel (Fe_2TiO_4). Mf, magnesioferrite ($MgFe_2O_4$). Sp, spinel ($MgAl_2O_4$). Hc, hercynite ($FeAl_2O_4$). Jc, jacobsite ($MnFe_2O_4$). Cr, chromite ($FeCr_2O_4$). Hm, hematite (Fe_2O_3). Ilm, ilmenite ($FeTiO_3$). Gk, geikielite ($MgTiO_3$). Py, pyrophanite ($MnTiO_3$). Es, eskolaite (Cr_2O_3).
[b]Number of cations assuming 3 cations per 4 oxygen (cubic oxides) and 2 cations per 3 oxygen (rhombohedral oxides).
[c]Interaction volume greater than spatial scale of exsolution. Composition is thus an average of the two exsolved phases.

order of decreasing volumetric abundance) in Batch 3 M-type samples is clinopyroxene, glass, plagioclase, and titanomagnetite. In T-type samples it is plagioclase, cliniopyroxene, glass, olivine, titanomagnetite, and ilmenite.

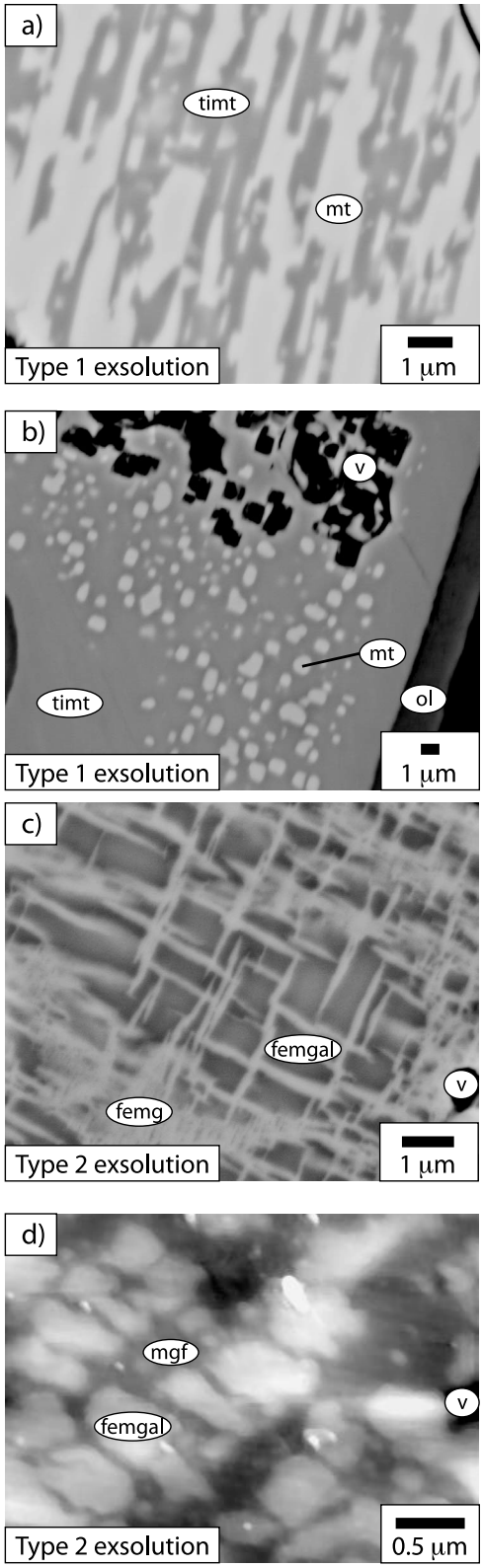

3.1.2. Compositions, Textures, and Oxidation State of Annealed Products

[14] Batches 1 and 2 of M-type annealed products have the same phase assemblage as the corresponding pre-anneal materials, with the exception of incipient devitrification of the glassy matrix at higher anneal temperatures and the following modifications of the oxide phases. While the pre-anneal materials contained both a cubic and a hematite-rich rhombohedral oxide, the annealed products contain only cubic oxides. Two texturally and compositionally distinct forms of exsolution are identified in the cubic oxides. Type 1 exsolution is defined as intergrowths of two phases along the magnetite (Mt)-ulvöspinel (Usp) solid solution, with minor Mg and Al ($Fe_{2.7}Ti_{0.1}Z_{0.2}O_4$–$Fe_{2.6}Ti_{0.3}Z_{0.1}O_4$). Phase boundaries are irregular, but appear to be crystallographically controlled, occurring preferentially on one of the host's {001} planes (Figure 2a). Compositional unmixing reflects preferential partitioning of Ti and Al into the titanomagnetite and Fe (and to a lesser extent, Mg) into the magnetite (Table 3). The relatively low amount of Mg and Al in the two phases suggests that hematite ($Fe_{1.7}Ti_{0.1}Z_{0.2}O_3$) was the corresponding pre-anneal phase. With decreasing anneal temperature, the spatial extent of the subordinate (magnetite-rich) phase decreases and becomes discontinuous (similar to that for Batch 3, Figure 2b). Type 2 exsolution lamellae occur on at least two {001} planes, at a considerably finer scale than Type 1 exsolution. Lamellae of exsolution type 2 phases are up to ~250 nm wide and are spaced at ~200–500 nm. Intergrowths are finer than the microprobe interaction volume, but a mixed-volume analysis of both phases yields a Fe-Mg-Al oxide ($Fe_{2.2}Mg_{0.4}Al_{0.2}Z_{0.2}O_4$) that is similar to the pre-anneal cubic phase (above). (Type 2 compositional partitioning is described below for T-type samples.) A few oxides did not undergo visible exsolution and have an average composition ($Fe_{2.1}Mg_{0.4}Al_{0.2}Z_{0.3}O_4$) similar to the pre-anneal cubic phase.

[15] Host crystals to both exsolution types as well as non-exsolved crystals contain pore spaces not present in the pre-anneal crystals (e.g., Figure 2b). These pores match the morphology of the exsolved phases, and we interpret this as resulting from subsolidus reaction.

[16] Batch 1 of the T-type anneal products are similar to the M-type products. Only cubic oxides are present, and they represent at least two texturally and compositionally distinct types of exsolution. One strongly resembles Type 1 Mt-Usp exsolution described above for the M-type samples. A second exsolution type strongly resembles Type 2 of the M-type composition, but in the T-type samples the lamellae spacing is slightly wider and more regular (Figure 2c). The phases are identified as Fe-Mg rich lamellae ($Fe_{2.4}Mg_{0.5}Z_{0.1}O_4$) in Fe-Mg-Al rich host ($Fe_{2.3}Mg_{0.3}Al_{0.3}Z_{0.1}O_4$), and the

Figure 2. Electron backscatter and AFM images demonstrating observed types of exsolution. (a) MAm-E-03, Type 1, Batch 1. (b) MAm-E-14, Type 1, Batch 3. (c) MB2-E-03, Type 2 (FeMg-FeMgAl), Batch 1. (d) MB2-E-03, Type 2 (Mf-FeMgAl), Batch 1. AFM image was processed using WsXM [*Horcas et al.*, 2007]. mt, magnetite; timt, titanomagnetite; ol, olivine; femg, Fe-Mg cubic oxide; femgal, Fe-Mg-Al cubic oxide; mgf, magnesioferrite; v, void or pore space.

compositional unmixing reflects preferential partitioning of Mg into the lamellae and Al into the host (Table 3). A (potentially) third exsolution type consists of Al-bearing magnesioferrite ($Fe_{1.9}Mg_{0.8}Al_{0.1}Z_{0.2}O_4$) lamellae in Fe-Mg-Al-rich ($Fe_{2.2}Mg_{0.5}Al_{0.2}Z_{0.1}O_4$) host (Figure 2d). Lamellae are slightly more irregular and the combined phases have more Mg and less Fe and Al than the Type 2 Fe-Mg – Fe-Mg-Al phase separation. However, in both cases, the intracrystal compositional variations are dominated by a negative correlation between Mg and Al, and the lamellae intersect at right angles. We therefore classify both textures as Type 2 exsolution. Non-exsolved crystals have a composition similar to that of the pre-anneal spinel oxide ($Fe_{2.0}Mg_{0.7}Al_{0.2}Z_{0.1}O_4$). The T-type Batch 2 anneal products contain no discernable exsolution textures.

[17] The Batch 3 annealed samples of both T-type and M-type compositions have phase assemblages similar to their pre-anneal material (plus the onset of glass devitrification), with the exception of the M-type sample annealed at 790°C (MAm-E-14). Many titanomagnetite crystals in this sample appear to have incipient Type 1 exsolution (Figure 2b), with a Mt-rich phase ($Fe_{2.7}Ti_{0.2}Z_{0.1}O_4$) exsolved in a Usp-rich host ($Fe_{2.2}Ti_{0.5}Al_{0.2}Z_{0.1}O_4$). The elemental partitioning is the same as that observed in the Batch 1 samples. All Batch 3 oxides (both cubic and rhombohedral) with no visible exsolution have compositions similar to the pre-anneal oxides. However, they contain relatively less Mg and more Fe, indicating subsolidus exchange of these elements with the matrix. Many of the cubic crystals (both exsolved and non-exsolved) also have a well-developed fayalitic (Fa_{87}) olivine rim, ~1–4 mm thick, which formed upon reaction with the glass phase during the subsolidus anneal treatment. Similar but more diffuse rims (of presumed similar composition) are present on the annealed samples of M-type Batch 1 oxide crystals.

3.2. Magnetics

3.2.1. Ordering Temperatures

[18] Changes in oxide mineral composition are reflected in changes in the measured ordering temperatures. Phases identified by microprobe cannot conclusively be linked to specific Curie temperatures (T_c) due to limited literature data on multicomponent solid solutions. Comparison with Curie temperatures of the relevant end-member compositions, however, allows us to place constraints on the data. Of the dominant end-members in our analyses (Table 3), ulvöspinel, hercynite, spinel, chromite, and ilmenite are all paramagnetic at and above room temperature. The Curie (or Néel) temperatures of magnetite and hematite are 580°C and 675°C, respectively, and the variations in ordering temperature within the magnetite-ulvöspinel and hematite-ilmenite solid solutions are well known [*Hunt et al.*, 1995]. The Curie temperature of jacobsite is ~300°C and that of magnesioferrite is often reported as 440°C [e.g., *Hunt et al.*, 1995], but equilibration at elevated temperatures can reduce this to <330°C [*O'Neill et al.*, 1992].

[19] Batch 1 and 2 (both M- and T-type) pre-anneal materials have two ordering temperatures at ~375–400°C and ~540°C, consistent with the Fe-Mg-Al cubic and the hematite-rich rhombohedral phase, respectively (Figure 3). The exception is the Batch 1 T-type material where the higher T_c is not evident. Batch 3 M-type and T-type pre-anneal materials each have a single T_C at ~300–375°C and ~140–180°C, respectively. Some replicate splits also have a higher T_C at ~485°C (M-type) and ~310°C (T-type). This heterogeneity is likely due to heterogeneity in the cubic phase arising from the fact that Batch 3 pre-anneal samples were synthesized in a much larger crucible which allowed for some crystal settling.

[20] After annealing, most samples that exhibit exsolution textures in BSE images also exhibit a change in Curie temperature(s) (Figure 3). When examining changes in ordering temperatures that accompany exsolution, we must keep in mind that reduction of the hematite to a cubic phase (Batches 1 and 2) would be accompanied by a reduction of T_C to ~350–375°C (assuming no changes in cation composition or stoichiometry). Figure 3 indicates the approximate Curie temperatures of the starting cubic phase(s) following reduction but prior to exsolution. The Batch 1 and 2 samples both demonstrate greater divergence from the pre-anneal T_c and greater spread between maximum and minimum T_c with increasing anneal temperature. This is suggestive of segregation into an Fe-rich and an Fe-poor phase(s), and that the extent of segregation is greater at higher temperatures. The exceptions are the Batch 2 T-type samples, where no visible exsolution was found. Batch 3 samples have less variability with respect to the pre-anneal materials. Both M-type samples have a slight decrease in T_c after annealing, with no significant difference between the sample that underwent visible exsolution (790°C) and the sample that did not (750°C). T-type samples have a T_c similar to that of the pre-anneal material.

3.2.2. Hysteresis and FORCs

[21] Compared to pre-anneal material, all annealed samples have an increase in coercivity and an increase in the ratio of saturation remanent magnetization (M_{rs}) to M_s (Figure 4). These increases are most dramatic in exsolved samples, and with increasing anneal temperature there is a shift away from single domain (SD) toward the multidomain (MD) end-member, suggesting that at higher anneal temperatures, exsolution microstructures coarsen more rapidly, resulting in a slightly decreased coercivity. In samples where no identifiable exsolution took place, the (relatively small) shift in domain-state could represent either fine-grained oxides that precipitated out of the glass and/or incipient exsolution that is too small to observe with the imaging techniques used.

[22] The interpretation of the observed higher remanence and coercivity in exsolved samples in terms of actual domain state is complex and non-unique. One possibility is that large homogeneous grains have been compositionally sub-divided into smaller, SD-like magnetic domains. This would require one of the exsolved phases be paramagnetic at room temperature or that exchange coupling is not continuous across phase boundaries. Because there are five to seven oxide phases present in the exsolved samples (Table 3), but only up to three observed Curie temperatures suggests that in some cases only one of the host/lamellae pair may be ferromagnetic. However, in other cases (such as Type 1 exsolution where both phases are relatively Fe-rich), both phases may be ferromagnetic. In this case the compositional boundaries may serve to pin domain walls or inhibit domain

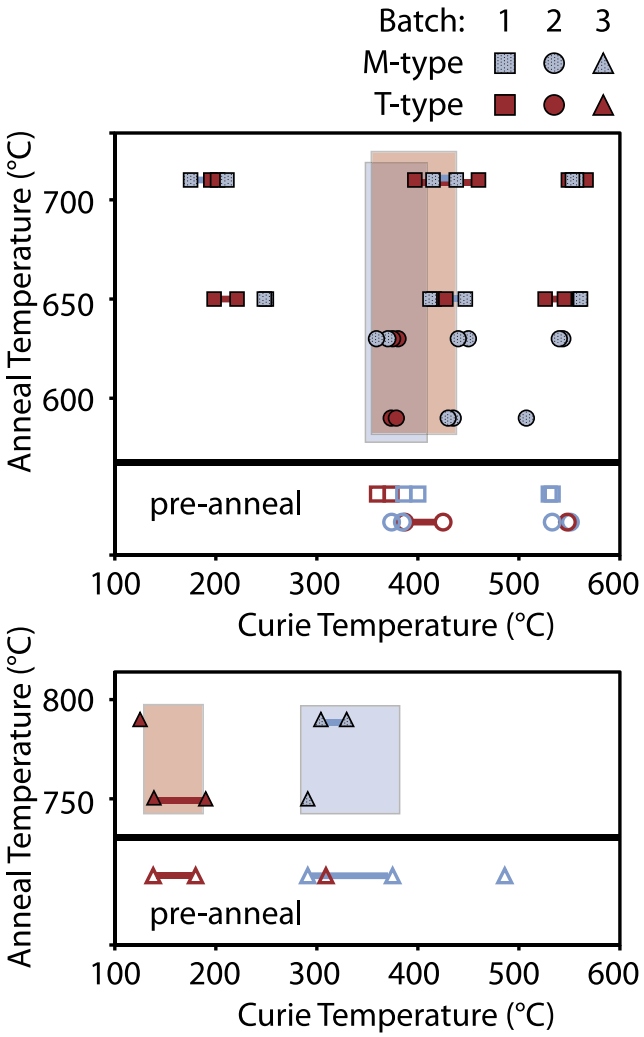

Figure 3. Curie temperature data for (top) Batches 1 and 2 and (bottom) Batch 3. Most samples with visible exsolution have significant deviation in Curie temperatures compared to the pre-anneal material. In most cases this is consistent with development of an Fe-rich and an Fe-poor phase(s). Open (closed) symbols are pre- (post-) anneal samples. Overlapping symbols or those connected by a bar are replicate measurements on separate splits. Shaded areas represent approximate range of Curie temperatures in pre-anneal material (following reduction in Batch 1 and 2 samples - see text) for comparison. In bottom plot, only the dominant T_C in pre-anneal material is indicated.

wall nucleation in a MD grain where exchange coupling is continuous across compositional boundaries. The increase in porosity in some annealed crystals may have a similar affect. MFM imaging did not definitively discriminate among these possibilities, but comparison of a pre-annealed MD grain (MB2–31) with an annealed, Type 2 exsolved (magnesioferrite −Fe-Mg-Al) grain demonstrates dramatic differences in magnetic structure, where within-grain magnetization is strongly correlated with composition in the exsolved grain (Figure S1). Regardless of the exact mechanism(s), it is clear that the exsolution results in a dramatic

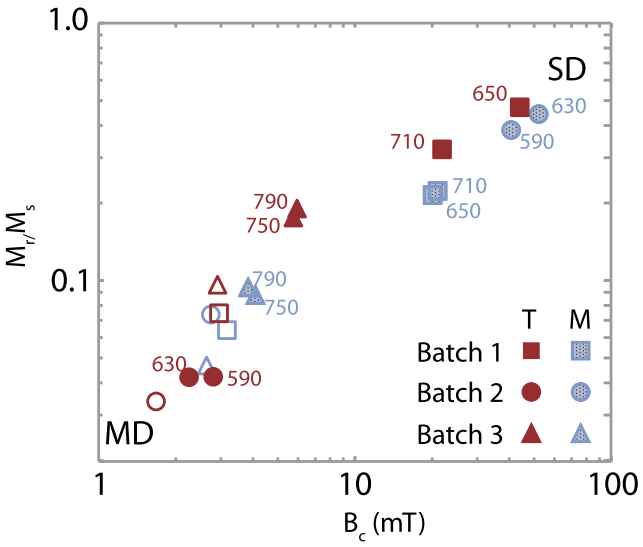

Figure 4. Hysteresis properties. Annealing treatments result in a reduction in effective magnetic grain size in all samples (shift toward SD end-member). This reduction is most pronounced in samples that underwent visible exsolution. Open symbols are pre- anneal samples. Closed symbols are post-anneal.

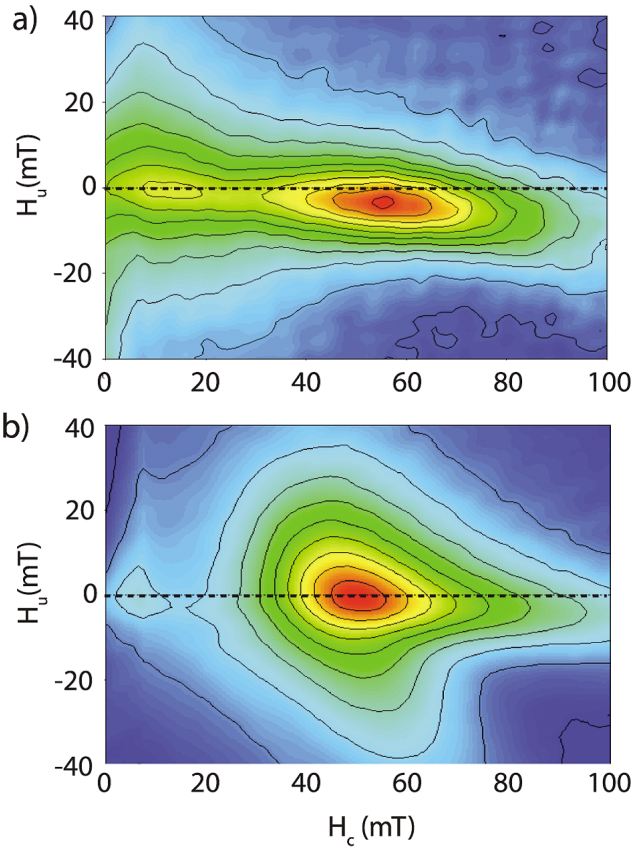

Figure 5. FORC diagrams for sample (a) MAm-E-03 (M-type, 710°C) and (b) MAm-E-06 (M-type, 590°C). Smoothing factor = 6. Data processed with FORCinel [*Harrison and Feinberg*, 2008].

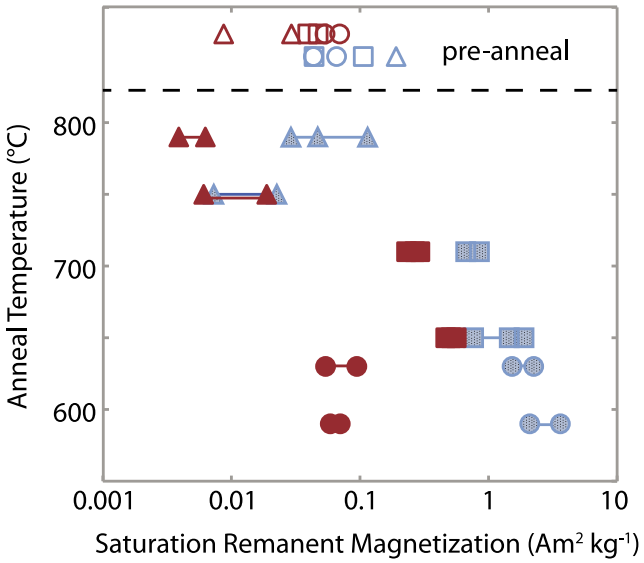

Figure 6. Saturation remanent magnetization as a function of anneal temperature. All Batch 1 and Batch 2 samples that underwent visible exsolution increase dramatically in saturation remanence. All Batch 3 samples decrease in saturation remanence, possibly through annealing out of crystal defects that can cause domain wall pinning. Symbols as in Figures 3 and 4. Overlapping symbols or those connected by a bar are replicate measurements on separate splits.

change in magnetic properties that should lead to stronger and more stable remanence.

[23] FORC distributions (Figure 5) are plotted with particle coercivity (H_c) along the horizontal axis, and interaction fields (H_u) are represented by spread along the vertical axis [*Pike et al.*, 1999]. All of the visibly exsolved Batch 1 and 2 samples have two distinct peaks in the FORC distribution: a low-coercivity (LC) peak centered at H_c = ~5–15 mT and a prominent high coercivity (HC) ridge that extends to ~100–120 mT (Figure 5a). The relative amplitude of the HC to LC ridges shown in Figure 5a is decreased from 1.4 at room temperature (Figure 5a) to 0.24 at 300°C, and at 510°C the HC ridge is not present. Because the high-T_C (>510°C) is likely associated with the magnetite-rich phase of the Type 1 exsolution, this demonstrates that the Type 1 exsolution is also associated with the LC peak, while the Type 2 exsolution is associated with the HC peak. This is consistent with EBS images (Figure 2), which show a coarser microstructure for the Type 1 exsolution.

[24] Only one of the exsolved samples (MAm-E-06, 590°C) is characterized by relatively high magnetostatic interaction, quantified by the full width at half maximum (FWHM) of a vertical profile through the FORC maximum. FWHM is ~35 mT for sample MAm-E-06 (Figure 5b), which is comparable to that in the naturally exsolved sample of *Evans et al.* [2006], and nearly twice that of the other Batch 1 and 2 samples (e.g., Figure 5a). This could arise from the relatively smaller scale of the exsolution and/or from a host-lamellae pair where one phase is paramagnetic, leading to increased magnetostatic interactions among the magnetic phase [*Harrison and Putnis*, 1997]. There are indeed only two Curie temperatures observed in this sample (compared to three in the sister samples annealed at higher temperatures), but it is unclear why only this sample would exsolve one paramagnetic phase. The microstructure of exsolved grains in this sample is very similar to that observed in MAm-E-14 (Figure 2b), but the size of the isolated regions of the subordinate phase are smaller (~0.2–0.5 μm).

3.2.3. Saturation Remanence

[25] All Batch 1 and Batch 2 samples that underwent visible exsolution increase dramatically in M_{rs}. M_{rs} increases with decreasing anneal temperature (Figure 6), suggesting a smaller, more stable domain configuration at lower anneal temperatures, consistent with both the hysteresis data and the images. On average, there is more within-sample heterogeneity in M_{rs} in the Batch 3 samples (Figure 6), and T-type samples cannot be distinguished from pre-anneal materials. Batch 3 M-type samples on average have a lower M_{rs} than the pre-anneal materials, perhaps through annealing out of crystal defects that can cause domain wall pinning. However, the single Batch 3 sample that did undergo visible exsolution (M-type, 790°C) has an elevated remanence compared to the unexsolved Batch 3 samples.

4. Discussion

4.1. Role of Reduction

[26] Because the Batch 1 and 2 samples underwent reduction during the anneal process, it is important to ascertain whether or not reduction was integral to the exsolution. This is most likely to affect the phases that started out as rhombohedral and converted to cubic structure during reduction (i.e., the Type 1 exsolution, Figures 2a and 2b). The prevalence of right angles at the boundaries between phases in these minerals is an indication that the cubic structure was present before exsolution began. Otherwise, the angular relationship between the lamellae would reflect superposition of cubic-to-cubic exsolution (restricted to {001} planes) on the trellis type ($\{111\}_{cubic}$ on $\{0001\}_{rhomb}$) texture that characterizes exsolution of a cubic phase from a rhombohedral host (compare oxyexsolution [*Haggerty*, 1991]). Additionally, Batch 1 and 2 (reduced from hematite) samples and Batch 3 (non-reduced) samples both underwent titanomagnetite (Type 1) exsolution and in some cases share a similar microstructure (e.g., Figure 2b). Finally, the solvus temperature in the hematite-ilmenite system is <525°C [*Burton and Davidson*, 1988; *Ghiorso*, 1997], suggesting that exsolution is unlikely to have begun in the rhombohedral state, unless the small amount of Mg in our phase (Table 3) raises this temperature considerably. We therefore infer that the change in fO_2 is not required for exsolution, and that the Batch 1 and 2 samples most likely transformed to cubic structure before undergoing exsolution. However, we cannot reject the possibility that the transformation from rhombohedral to cubic structure introduces defects that provide energetically advantageous sites for nucleation of lamellae, allowing exsolution to occur more readily in the Batch 1 and 2 samples.

[27] We also briefly note that the Fe/Al-rich (M-type) and Fe/Al-poor (T-type) synthetic basalts contain similar Fe-Ti-Al-Mg oxides which undergo texturally and magnetically indistinguishable exsolution upon anneal, suggesting that

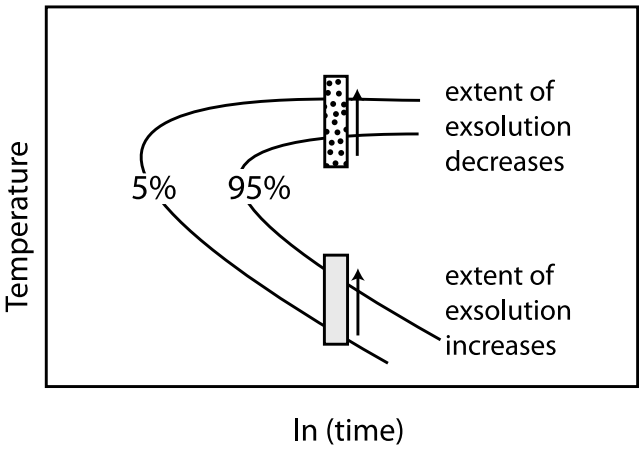

Figure 7. Partially schematic TTT diagram describing the relative kinetics of transformation as a function of cooling. Progress toward equilibrium is depicted as two C-shaped curves representing incipient (5%) and nearly complete (95%) stages of the process. Observation of increasing extent of unmixing (with respect to compositions of lamellae phases) with increasing temperature suggests experiments were performed at the light gray shaded region. The opposite trend would be expected in the stippled region.

(at least at high degrees of oxidation) oxygen fugacity exerts a more important control on oxide mineralogy than the composition of the silicate melt from which crystals form.

4.2. Constraints on Multicomponent Solvus

[28] The fact that a greater divergence in Curie temperatures is observed with increasing anneal temperature in the Batch 1 and 2 samples indicates that the exsolution process has proceeded further toward completion at higher temperatures, in spite of the fact that anneal times are somewhat shorter. Whereas equilibrium phase separation along a hoop-shaped solvus would cause increasing phase compositional separation with decreasing temperature, the T_c data, particularly for the Fe-poor phases (Figure 3), suggest that the increased reaction rates afforded by higher temperatures dominate the extent of unmixing that can occur on the laboratory time scale. This observation, viewed in the context of a classical time-temperature-transformation (TTT) plot (shown schematically in Figure 7), suggests that the anneal temperatures are low relative to the temperatures at which the exsolution rate would be maximized. In turn, this suggests our anneal temperatures are well beneath the solvus, at least for the Batch 1 and 2 compositions. We briefly note that observed exsolved compositions are not interpreted to represent solvus limb compositions at equilibrium. Rather, the compositions are likely related to the kinetics associated with the specific mechanism of exsolution and illustrate the need for longer-duration experiments to constrain actual solvus shape.

[29] Because only one Batch 3 sample underwent exsolution, we can place fewer constraints on the solvus for this oxide composition. However, this sample demonstrates some of the complexities of a multicomponent solvus. Even the relatively small amount of Mg and Al in the Batch 3 titanomagnetite (Table 3) is enough to raise the consolute temperature from $<\sim$600°C to at least 790°C. Because this is well above the Curie temperature of all cubic oxide phases, multicomponent cubic oxides that undergo exsolution via slow cooling should carry dominantly a TRM.

5. Conclusions

[30] We have successfully induced cubic-cubic exsolution in cubic Fe-oxides of a variety of compositions. Fine-scale intergrowths of magnetite-rich and magnetite-poor Fe-Ti-Al-Mg oxides, interpreted to represent cubic phase exsolution, were observed in seven samples, one that was synthesized and annealed at approximately constant fO_2 (QFM) and six that were synthesized at very oxidizing conditions (corresponding to $\sim$QFM +6) and annealed at less oxidizing conditions. Results demonstrate that:

[31] 1. Compositions near the magnetite-ulvöspinel solid solution exsolved by preferentially partitioning Ti and Al into a titanomagnetite-rich host and Fe (and to a lesser extent Mg) into a magnetite-rich subordinate phase. In our experiments this Type 1 exsolution resulted in irregular (but crystallographically controlled) phase boundaries.

[32] 2. Compositions with greater amounts of Mg and Al are characterized by relative partitioning of Mg into the lamellae and Al into the host and by regular, continuous lamellae intersecting at right angles along the crystallographic {001} planes.

[33] 3. With increasing anneal temperature, Curie temperature data in most exsolved samples show greater divergence from pre-anneal materials and greater divergence between the maximum and minimum T_c. This suggests that the exsolution process has proceeded further toward completion at higher temperatures, which in turn suggests that anneal temperatures are well below the solvus for our compositions.

[34] 4. Coercivity and saturation remanent magnetization dramatically increase in most exsolved samples, demonstrating that this type of exsolution can exert strong control on the strength and stability of magnetization. The increase in remanence likely arises from a change in the domain state of the oxides, which may result from compositional subdivision into smaller magnetic domains and/or via inhibition of domain wall nucleation or pinning of walls on compositional boundaries. A shift away from single domain toward the multidomain state with increasing anneal temperature (Batch 1 and 2) reflects more rapid coarsening of the microstructure at higher temperatures. This suggests that both the time and temperature at which basalts undergo exsolution in nature can play a dramatic role in the resulting magnetization.

[35] 5. Because the consolute temperature of the multicomponent systems lies far above the Curie temperatures of all cubic spinels, basalts bearing this type of exsolution can carry a total or near total TRM if the bulk of the process takes place above 580°C.

[36] **Acknowledgments.** Many thanks to Richard Harrison and David Krasa, whose reviews improved and clarified the manuscript. Support for this work was provided by NASA MFRP award NNG05GL92G to J.E.H. Part of the work was carried out during a Visiting Fellowship to the Institute for Rock Magnetism (IRM) by L.T.-P. This is IRM contribution 1107. The IRM receives support from the Instrumentation and Facilities program of the National Science Foundation, Earth Science Division, and from the University of Minnesota.

References

Andersen, D. J., D. H. Lindsley, and P. M. Davidson (1993), QUILF: A Pascal program to assess equilibria among Fe-Mg-Mn-Ti oxides, pyroxenes, olivine, and quartz, *Comput. Geosci.*, *19*, 1333–1350, doi:10.1016/0098-3004(93)90033-2.

Bowles, J., J. Hammer, and S. Brachfeld (2009), Magnetic and petrologic characterization of synthetic Martian basalts and implications for the surface magnetization of Mars, *J. Geophys. Res.*, *114*, E10003, doi:10.1029/2009JE003378.

Brachfeld, S., and J. Hammer (2006), Rock-magnetic and remanence properties of synthetic Fe-rich basalts: Implications for Mars crustal anomalies, *Earth Planet. Sci. Lett.*, *248*, 599–617, doi:10.1016/j.epsl.2006.04.015.

Burton, B. P., and P. M. Davidson (1988), Multicritical phase relations in minerals, *Adv. Phys. Geochem.*, *7*, 60–90, doi:10.1007/978-1-4612-3862-1_4.

Deer, W. A., R. A. Howie, and J. Zussman (1962), *Rock-Forming Minerals*, vol. 5, *Non-Silicates*, 371 pp., John Wiley, New York.

de Faria, D., S. Venâncio Silva, and M. T. De Oliveira (1997), Raman microspectroscopy of some iron oxides and oxyhydroxides, *J. Raman Spectrosc.*, *28*, 873–878, doi:10.1002/(SICI)1097-4555(199711)28:11<873::AID-JRS177>3.0.CO;2-B.

Droop, G. T. R. (1987), A general equation for estimating Fe^{3+} concentrations in ferromagnesian silicates and oxides from microprobe analyses, using stoichiometric criteria, *Mineral. Mag.*, *51*, 431–435, doi:10.1180/minmag.1987.051.361.10.

Evans, M. E., D. Krasa, W. Williams, and M. Winklhofer (2006), Magnetostatic interactions in a natural magnetite-ulvospinel system, *J. Geophys. Res.*, *111*, B12S16, doi:10.1029/2006JB004454.

Frost, B., and D. H. Lindsley (1991), Occurrence of iron-titanium oxides in igneous rocks, *Rev. Mineral. Geochem.*, *25*, 433–468.

Genge, M. J., and M. M. Grady (1999), The fusion crusts of stony meteorites: Implications for the atmospheric reprocessing of extraterrestrials materials, *Meteorit. Planet. Sci.*, *34*, 341–356, doi:10.1111/j.1945-5100.1999.tb01344.x.

Ghiorso, M. S. (1997), Thermodynamic analysis of the effect of magnetic ordering on miscibility gaps in the FeTi cubic and rhombohedral oxide minerals and the FeTi oxide geothermometer, *Phys. Chem. Miner.*, *25*, 28–38, doi:10.1007/s002690050083.

Golla-Schindler, U., H. S. C. O'Neill, and A. Putnis (2005), Direct observation of spinodal decomposition in the magnetite-hercynite system by susceptibility measurements and transmission electron microscopy, *Am. Mineral.*, *90*(8–9), 1278, doi:10.2138/am.2005.1849.

Grommé, C., T. Wright, and D. Peck (1969), Magnetic properties and oxidation of iron-titanium oxide minerals in Alae and Makaopuhi lava lakes, Hawaii, *J. Geophys. Res.*, *74*, 5277–5293, doi:10.1029/JB074i022p05277.

Haggerty, S. E. (1991), Oxide textures—A mini-atlas, in *Oxide Minerals: Petrologic and Magnetic Significance*, edited by D. H. Lindsley, pp. 129–219, Mineral. Soc. of Am., Chelsea, Mich.

Hammer, J., M. Coombs, P. Shamberger, and J. Kimura (2006), Submarine sliver in north Kona: A window into the early magmatic and growth history of Hualalai Volcano, Hawaii, *J. Volcanol. Geotherm. Res.*, *151*, 157–188, doi:10.1016/j.jvolgeores.2005.07.028.

Hargraves, R. B., J. M. Knudsen, M. B. Madsen, and P. Bertelsen (2001), Finding the right rocks on Mars, *Eos Trans. AGU*, *82*, 292.

Harrison, R., and J. Feinberg (2008), FORCinel: An improved algorithm for calculating first-order reversal curve distributions using locally weighted regression smoothing, *Geochem. Geophys. Geosyst.*, *9*, Q05016, doi:10.1029/2008GC001987.

Harrison, R. J., and A. Putnis (1997), Interaction between exsolution microstructures and magnetic properties of the magnetite-spinel solid solution, *Am. Mineral.*, *82*(1–2), 131–142.

Harrison, R. J., and A. Putnis (1998), The magnetic properties and crystal chemistry of oxide spinel solid solutions, *Surv. Geophys.*, *19*, 461–520, doi:10.1023/A:1006535023784.

Horcas, I., R. Fernandez, J. M. Gomez-Rodriguez, J. Colchero, J. Gomez-Herrero, and A. Baro (2007), WSXM: A software for scanning probe microscopy and a tool for nanotechnology, *Rev. Sci. Instrum.*, *78*, 013705, doi:10.1063/1.2432410.

Hunt, C. P., B. M. Moskowitz, and S. K. Banerjee (1995), Magnetic properties of rocks and minerals, in *Rock Physics and Phase Relations: A Handbook of Physical Constants*, edited by T. J. Ahrens, pp. 189–204, AGU, Washington, D. C., doi:10.1029/RF003p0189.

Johnston, A. D., and J. H. Stout (1984), A highly oxidized ferrian salite-, kennedyite-, forsterite-, and rhönite-bearing alkali gabbro from Kauai, Hawaii and its mantle xenoliths, *Am. Mineral.*, *69*, 57–68.

Joy, D. C. (2001), Fundamental constants for quantitative X-ray microanalysis, *Microsc. Microanal.*, *7*, 159–167.

Kawai, N. (1956), Exsolution of titanomagnetites and its effect on rock-magnetism, *Proc. Jpn. Acad.*, *32*, 464–468.

Lindsley, D. H. (1981), Some experiments pertaining to the magnetite-ulvospinel miscibility gap, *Am. Mineral.*, *66*, 759–762.

Llovet, X., and G. Galan (2003), Correction of secondary X-ray fluorescence near grain boundaries in electron microprobe analysis: Application to thermobarometry of spinel lherzolites, *Am. Mineral.*, *88*, 121–130.

Mattioli, G. S., and B. J. Wood (1988), Magnetite activities across the $MgAl_2O_4$-Fe_3O_4 spinel join, with application to thermobarometric estimates of upper mantle oxygen fugacity, *Contrib. Mineral. Petrol.*, *98*, 148–162, doi:10.1007/BF00402108.

O'Neill, H., H. Annersten, and D. Virgo (1992), The temperature-dependence of the cation distribution in magnesioferrite ($MgFe_2O_4$) from powder XRD structural refinements and Mossbauer-spectroscopy, *Am. Mineral.*, *77*, 725–740.

Pike, C. R., A. P. Roberts, and K. L. Verosub (1999), Characterizing interactions in fine magnetic particle systems using first order reversal curves, *J. Appl. Phys.*, *85*, 6660–6667, doi:10.1063/1.370176.

Price, G. (1980), Exsolution microstructures in titanomagnetites and their magnetic significance, *Phys. Earth Planet. Inter.*, *23*, 2–12, doi:10.1016/0031-9201(80)90078-3.

Price, G. D. (1981), Subsolidus phase-relations in the titanomagnetite solid-solution series, *Am. Mineral.*, *66*, 751–758.

Reed, S. J. B. (1993), *Electron Microprobe Analysis*, 2nd ed., 91 pp., Cambridge Univ. Press, Cambridge, U. K.

Shi, G. H., P. Tropper, and R. X. Zhu (2009), The occurrence of magnesioferrite-rich spinels in a trachyandesite from NE China, *Mineral. Petrol.*, *95*, 125–134, doi:10.1007/s00710-008-0025-2.

Smit, J. (1999), The global stratigraphy of the Cretaceous-Tertiary boundary impact ejecta, *Annu. Rev. Earth Planet. Sci.*, *27*, 75–113, doi:10.1146/annurev.earth.27.1.75.

Tamura, A., and S. Arai (2005), Unmixed spinel in chromitite from the Iwanai-dake peridotite complex, Hokkaido, Japan: A reaction between peridotite and highly oxidized magma in the mantle wedge, *Am. Mineral.*, *90*, 473–480, doi:10.2138/am.2005.1570.

Turnock, A. C., and H. Eugster (1962), Fe-Al oxides: Phase relationships below 1,000°C, *J. Petrol.*, *3*, 533–565.

Vincent, E., J. Wright, R. Chevallier, and S. Mathieu (1957), Heating experiments on some natural titaniferous magnetites, *Mineral. Mag.*, *31*, 624–655, doi:10.1180/minmag.1957.31.239.03.

Wang, A., K. E. Kuebler, B. L. Jolliff, and L. A. Haskin (2004), Raman spectroscopy of Fe-Ti-Cr-oxides, case study: Martian meteorite EETA79001, *Am. Mineral.*, *89*, 665–680.

Wood, B. J., and D. Virgo (1989), Upper mantle oxidation state: Ferric iron contents of Iherzolite spinels by 57 Fe Mössbauer spectroscopy and resultant oxygen fugacities, *Geochim. Cosmochim. Acta*, *53*, 1277–1291, doi:10.1016/0016-7037(89)90062-8.

Zinin, P., L. Tatsumi-Petrochilos, L. Bonal, T. Acosta, J. Hammer, S. Gilder, and M. Fuller (2011), Raman spectroscopy of the titanomagnetites: Calibration of the intensity of Raman peaks as a sensitive indicator of Ti content, *Am. Mineral.*, *96*, 1537–1546, doi:10.2138/am.2011.3745.

J. A. Bowles, Institute for Rock Magnetism, Department of Earth Sciences, University of Minnesota, Twin Cities, 310 Pillsbury Dr. SE, Rm. 108, Minneapolis, MN 55455-0231, USA. (jbowles@umn.edu)

S. A. Brachfeld, Department of Earth and Environmental Studies, Montclair State University, Upper Montclair, NJ 07043, USA.

J. E. Hammer and L. Tatsumi-Petrochilos, Department of Geology and Geophysics, University of Hawai'i at Mānoa, 1680 East-West Rd., Honolulu, HI 96822, USA.